

Damaged Area Mapping and Ground Displacement Estimation using Sentinel-1 Synthetic Aperture Radar (SAR) Interferometry: January 12, 2020, Taal Volcano Eruption Case Study, Philippines

Ryan A. Ramirez* and Rajiv Eldon E. Abdullah

Department of Civil Engineering
University of Santo Tomas
Sampaloc, Manila 1008 Philippines

*rramirez@ust.edu.ph

Date received: September 25, 2021

Revision accepted: September 20, 2022

Abstract

The availability of damage assessment maps and ground displacement information is essential in the Philippines, which experiences various types of climate-induced and naturally-driven geohazards. The emergence of freely accessible space-borne synthetic aperture radar (SAR) data has led to interferometric SAR (InSAR) applications in the Philippines. However, most InSAR studies only focused on ground displacement detection, monitoring, and modeling and not on damages resulting from geohazards. This work used pre- and co-eruption Sentinel-1 interferometric pair datasets and the SeNtinel-1 Application Platform tool to create a pixel-based damage proxy map (DPM) for the 2020 Taal Volcano eruption in the Philippines, employing a coherence difference analysis. The pre-eruption coherence difference data stack mean and standard deviation were exploited to achieve a coherence difference threshold that reasonably created the DPM that delineated damaged areas, which included buildings and roads. The DPM was qualitatively evaluated through comparison with the field investigation and reports obtained from the Philippine Institute of Volcanology and Seismology (PHIVOLCS) and showed significant agreement with 89% overall accuracy. The decomposition of the line-of-sight displacement field map revealed the dynamic geological activities due to the phreatomagmatic eruption. The vertical displacements from InSAR and in-situ measurements obtained from field inspection and PHIVOLCS reports showed excellent agreement with root-mean-squared less than 2 cm and coefficient of determination (R^2) close to unity. Overall, the application of InSAR to Sentinel-1 SAR images successfully mapped damaged areas and estimated ground displacements associated with the Taal Volcano phreatomagmatic eruption on January 12, 2020.

Keywords: coherence difference analysis, ground displacement, InSAR, Sentinel-1, Taal Volcano eruption

1. Introduction

On January 12, 2020, a phreatomagmatic eruption occurred from the primary crater of the active Taal Volcano in Batangas City, Philippines. Before the eruption, the Philippine Institute of Volcanology and Seismology (PHIVOLCS) had issued Alert Level 1 on the volcano due to anomalous volcanic activities (PHIVOLCS, 2019). In November 2019, PHIVOLCS recorded 57 volcanic earthquakes, which resulted in an escalated danger warning from Alert Level 2 to 4. In February 2020, the danger warning was downgraded to Alert Level 2 after observing a consistent decrease in volcanic activities.

Monitoring active volcanoes and seismic-prone areas and forecasting any untoward event, resulting from volcanic eruptions and earthquakes, are critical in the Philippines. Several field instruments and ground-based geodetic and geophysical techniques for studying these areas have been used extensively (Lowry *et al.*, 2001; Bartel *et al.*, 2003; Fikos *et al.*, 2012; Galgana *et al.*, 2014; Kumagai *et al.*, 2014; Zlotnicki *et al.*, 2017). However, these methods include point-specific measurements and only have limited area coverage. In the last three decades, the interferometric synthetic aperture radar (InSAR) technique has been profitably employed to detect ground surface displacements due to natural geological hazards and identify hazard-induced disasters in urban and natural environments (Bürgmann *et al.*, 2000; Massonnet and Sigmundsson, 2000; Zebker *et al.*, 2000; Fernández *et al.*, 2002; Wauthier *et al.*, 2009; Baker and Amelung, 2012). InSAR has emerged as a viable remote sensing technique for emergency response, disaster monitoring and crisis management in spatiotemporal dimensions. InSAR has been enormously applied for quantifying earthquake-induced surface displacements (Moro *et al.*, 2017; Chen *et al.*, 2019; Li *et al.*, 2020; Liu *et al.*, 2021) and volcanic eruption-induced ground deformations (Kubaneck *et al.*, 2015; Jung *et al.*, 2016; Nobile *et al.*, 2017; Doke *et al.*, 2018). Additionally, InSAR has been effectively utilized for volcano observations and monitoring (Ebmeier *et al.*, 2018; Wang *et al.*, 2018; Garthwaite *et al.*, 2019; Hamling, 2021; Di Traglia *et al.*, 2021). Most of these InSAR studies only focused on ground surface deformation detection and quantification, monitoring and modeling and not on associated damages (i.e., mapping damaged buildings, houses and road pavements) resulting from the eruptive activities of volcanoes. Prasetyo *et al.* (2021) showed that eruption and evacuation characteristics are two essential factors concerning how people respond to a volcano eruption; however, asset damage had the highest effect on response

action, at least during the 2020 Taal Volcano eruption. Hence, a cost-efficient and quick mapping method of asset damage, overcoming the danger posed by the volcanic activities (i.e., before, during, and after the eruption), is imperative in emergency response coordination.

Despite the successful applications of InSAR in other regions concerning volcanism, the Philippines is behind in utilizing archived SAR data and open-source, freely distributed remote sensing tools. Morales Rivera *et al.* (2015) used SAR data acquired by the Advanced Land Observing Satellite-1 (ALOS-1) ascending orbit from the Japanese Aerospace Exploration Agency to monitor and model the volcanic unrest of four active volcanoes (i.e., Bulusan, Kanlaon, Mayon and Taal) in the Philippines from 2007-2011. Mabaquiao (2021) processed a pair of SAR data acquired by the descending Sentinel-1A satellite to quantify the ground surface deformation of Metro Manila before and after the eruption of Taal Volcano in January 2020. On the one hand, Bato *et al.* (2021) explored SAR data stacks acquired by ascending and descending ALOS-PALSAR 2 and Sentinel-1A/B satellite missions to quantify and model the pre-, co- and post-eruptive state of the 2020 Taal Volcano eruption. However, these previous studies on volcanism-induced ground surface deformation investigations primarily used the interferometric phase setting aside the InSAR coherence commonly used to assess the quality of the InSAR-derived displacement measurements. Coherence indicates the consistency in data between two coregistered SAR images. Therefore, the coherence difference between two interferometric pairs can isolate surface changes related to disastrous events. However, the complex InSAR processing involved has restricted research efforts in the Philippines to apply the coherence difference analysis between pre- and post-event SAR image pairs even though the country frequently experiences other climate-induced and naturally-driven geohazards such as landslides and earthquakes (Ramirez, 2021; Abcede *et al.*, 2022; Tiongson and Ramirez, 2022). The unprecedented availability of free Sentinel-1 SAR images provided through the Copernicus Programme of the joint initiative of the European Space Agency (ESA) and European Commission (EC); thus, motivated this study to apply interferometric phase and coherence difference analyses to investigate the spatial distribution of damages incurred after the Taal Volcano eruption on January 12, 2020.

In this present work, SAR datasets acquired by the ascending and descending Sentinel-1 satellites were processed using the SeNtinel-1 Application Platform (SNAP) tool to obtain a co-eruption damage proxy map (DPM) in Taal

Volcano island and its adjoining towns. This work utilized the interferometric pair coherence before and after the eruption and estimated the horizontal and vertical directional components of ground surface displacements after unwrapping the differential interferograms. Specifically, the pre-eruption coherence difference data stack mean and standard deviation were exploited to achieve a coherence difference threshold to improve the DPM creation. The DPM and InSAR vertical displacements were compared with the ground truth acquired from field inspections and reports from PHIVOLCS.

2. Methodology

2.1 Description of Study Area

Taal Volcano, designated as Decade Volcanoes, is the Philippines' second most active volcano, located in the province of Batangas ($14^{\circ} 0' 36''$ N, $129^{\circ} 59' 51''$ E) (Figure 1). It is a large caldera formed from prehistoric eruptions between 140,000 and 5,380 BP (Before Present) (Delos Reyes *et al.*, 2018). In records, 33 eruptions, excluding the most recent one, had been reported on Volcano Island, located in Taal Lake. On January 12, 2020, Taal Volcano erupted from its primary crater. CALABARZON Region (i.e., Cavite, Laguna, Batangas, Rizal, and Quezon), the National Capital Region (i.e., Metro Manila), and some parts of Region III and Ilocos Region were cloaked with volcanic ash deposits. The imminent danger related to the volcanic unrest before the eruption resulted in class and work suspensions and flight cancellations in the Taal area. The following day, January 13, 2020, a lava fountain occurred after the volcano emitted a weak Strombolian eruption. PHIVOLCS registered roughly 2,500 seismic activities of the volcanic-tectonic type in the Taal area. Figures 1b to 1e display the documented ground fissures in the adjoining towns of the Taal Volcano island, which are encompassed in the 15-km radius danger zone.

On January 15, 2020, the water in the central crater and the Pansipit River drained. The water loss in the Pansipit River was associated with the upward movement of the magma that caused widespread ground fissures in the surrounding towns. On January 26, 2020, PHIVOLCS lowered the danger warning from Alert Level 4 to 3 due to decreasing volcanic activity in Taal. Small volcanic earthquakes with magnitudes 1.5 to 2.2 were recorded from January 27-28, 2020 with no perceived event.

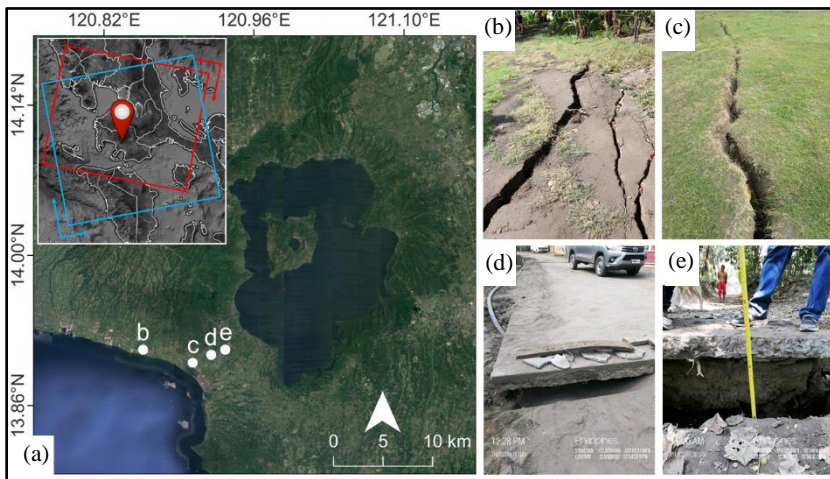


Figure 1. Inset in (a) locates the region of interest in the Philippines. The footprints of Sentinel-1A/B images used in this study are marked with the red square (descending track) and blue square (ascending track). The background is a Google Earth satellite image (Google, n.d.). Photos (b-e) show multiple and large ground fissures that appeared in different towns of Batangas during the 2020 Taal Volcano eruption.

2.2 Sentinel-1 SAR Datasets

Sentinel-1 satellites supplied the Single-Look-Complex (SLC) SAR products used in this study. Sentinel-1 is loaded with a C-band radar sensor with a 5.6 cm wavelength. The collected SAR datasets were acquired in the Interferometric Wide (IW) swath mode having co-vertical (VV) polarization. Sentinel-1 is a near-polar orbit twin satellite constellation. Thus, Sentinel-1 traverses over the same region of interest from north to south (descending track) and south to north (ascending track). Each satellite (Sentinel-1A and Sentinel-1B) has a 12-day revisit period and an effective six-day revisit period together. The data have been freely provided since 2016. ESA and EC jointly operate the Sentinel-1 missions under Copernicus Programme. The Terrain Observation by Progressive Scans SAR (TOPSAR) technology is the primary acquisition mode of Sentinel-1 missions. TOPSAR supplies a SAR image with 250 x 200 km area coverage. SAR products comprise three swaths (IW1-IW3) consisting of a series of bursts. The 20 x 5 m spatial resolution (azimuth x range directions) allows for more precise monitoring of the target area. Sentinel-1 Precise Orbit Ephemerides (POE) update the satellite position and velocity information in the metadata of procured SAR products.

Table 1 summarizes the immediate pre- and co-eruption interferometric pairs defined from the SAR images captured by the ascending and descending Sentinel-1 satellites after the volcano eruption. Figure 2 shows the temporal (Btemp) and perpendicular (Bperp) baselines of all datasets used for InSAR analysis.

Table 1. Pre-eruption and co-eruption interferometric pairs information for ascending and descending data stack

ID no.	Master scene	Slave scene	Btemp (days)	Bperp (m)	Track	Event type
AP	20191230	20200111	12	41	Ascending	Pre-eruption
AC	20200111	20200117	6	-6	Ascending	Co-eruption
DP	20191228	20200109	12	-28	Descending	Pre-eruption
DC	20200109	20200115	6	-68	Descending	Co-eruption

The time format of all acquired SAR images is provided as *yyyymmdd*. Letters A and D denote ascending and descending tracks. Letters P and C denote pre-eruption and co-eruption time windows.

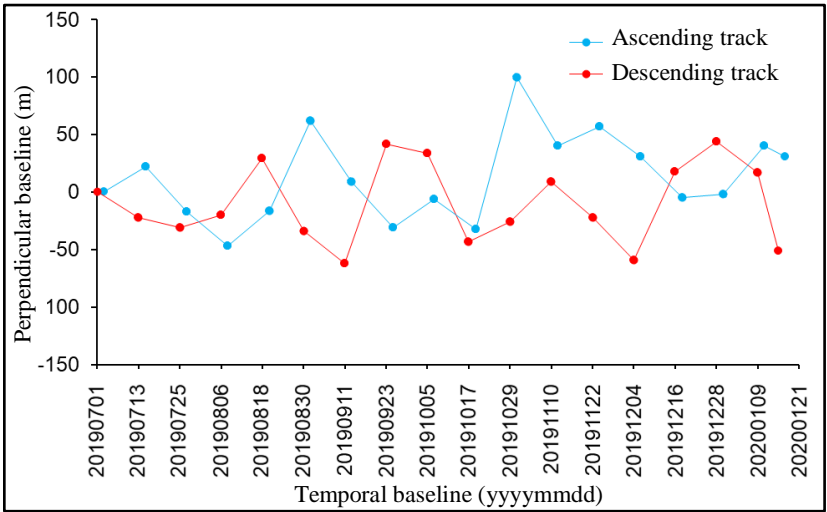


Figure 2. Perpendicular baseline information was presented concerning the first SAR acquisition for each track. Solid lines mark 12 days between consecutive SAR image acquisitions for pre-eruption interferometric pairs and six days for co-eruption interferometric pairs for ascending and descending data stack.

This study collected 36 Sentinel-1 SAR data from July 1, 2019 to January 17, 2020 (18 images each from ascending and descending tracks). The Sentinel-1 SAR data were processed to generate 34 coherence images (Tables 1, 2 and

3). The coherence difference threshold was determined by exploiting pre-eruption coherence difference data stack mean and standard deviation (i.e., 32 out of 34 coherence images) to mitigate background effects further. The reference pre-eruption images were pairs AP for the ascending data stack and DP for the descending data stack.

Table 2. The information on pre-eruption interferometric pairs for the ascending track

ID no.	Master scene	Slave scene	Btemp (days)	Bperp (m)
A-01	20190703	20190715	12	22
A-02	20190715	20190727	12	-38
A-03	20190727	20190808	12	-33
A-04	20190808	20190820	12	32
A-05	20190820	20190901	12	79
A-06	20190901	20190913	12	-54
A-07	20190913	20190925	12	-39
A-08	20190925	20191007	12	26
A-09	20191007	20191019	12	-27
A-10	20191019	20191031	12	132
A-11	20191031	20191112	12	-59
A-12	20191112	20191124	12	16
A-13	20191124	20191206	12	-26
A-14	20191206	20191218	12	-36
A-15	20191218	20191230	12	4

Table 3. The information on pre-eruption interferometric pairs for the descending track

ID no.	Master scene	Slave scene	Btemp (days)	Bperp (m)
D-01	20190701	20190713	12	-23
D-02	20190713	20190725	12	-8
D-03	20190725	20190806	12	9
D-04	20190806	20190818	12	51
D-05	20190818	20190830	12	-63
D-06	20190830	20190911	12	-29

Table 3 continued.

D-07	20190911	20190923	12	104
D-08	20190923	20191005	12	-7
D-09	20191005	20191017	12	-79
D-10	20191017	20191029	12	19
D-11	20191029	20191110	12	35
D-12	20191110	20191122	12	-32
D-13	20191122	20191204	12	-36
D-14	20191204	20191216	12	77
D-15	20191216	20191228	12	26

2.3 InSAR-based Change Detection

SAR instruments work by emitting a pulse and then measuring the intensity of the phase and the time of return from the signal after it bounces off the surface. The backscattered radar signals are employed to create imagery containing amplitude (A) and phase (φ) information. The amplitude is expressed in dB, whereas the phase is in terms of radians. The information is stored in the metadata of the SAR product as complex numbers. The phasor (P) per pixel containing this information is expressed in Equation 1 (Strozzi *et al.*, 2002).

$$P = Ae^{i\varphi} \quad (1)$$

where i is the imaginary unit. Moreover, the amplitude is a measure of the backscattered signal strength, and the phase is the fraction of one complete sinusoidal signal. The range between the radar sensor and the ground targets primarily determines the SAR image's phase information.

The main principle of any InSAR technique is through interference between two constructed SAR scenes captured at distant times over the same region creating a so-called interferogram. The interferogram is created by cross multiplying the slave image (e.g., post-eruption image) complex conjugate to the master image (e.g., pre-eruption image). Specifically, the amplitude of two SAR images is multiplied, whereas the phase difference ($\Delta\varphi$) expresses the interferometric phase value between the two images as described in Equation 2.

$$P_1 P_2^* = A_1 A_2 e^{i(\varphi_1 - \varphi_2)} \quad (2)$$

where P_1 and P_2 represent the master and slave scenes and * indicates complex conjugation. The interferometric phase can have phase error contributions from five different sources as described in Equation 3.

$$(\varphi_1 - \varphi_2) = \Delta\varphi = \Delta\varphi_{flat} + \Delta\varphi_{topo} + \Delta\varphi_{disp} + \Delta\varphi_{atm} + \Delta\varphi_{noise} \quad (3)$$

where $\Delta\varphi_{flat}$ is the phase error due to the curvature of the earth, $\Delta\varphi_{topo}$ is the topographic error (i.e., digital elevation model [DEM] error), $\Delta\varphi_{disp}$ is the surface deformation error, $\Delta\varphi_{atm}$ is the atmospheric error and $\Delta\varphi_{noise}$ is the phase noise introduced due to temporal change of ground targets, distinct side-looking angle and volume scattering. Through interferometry, other phase errors are eliminated and only focus on the phase contributor of interest, which in this study was the surface deformation.

2.4 Damage Proxy Map Creation using Coherence Difference Analysis

Not every pixel in a space-borne SAR image for damage assessment and ground displacement estimation provides practical phase information. The successful employment of SAR images in any earth observation purpose processed with any InSAR technique relies on coherence (γ). When ground targets move between two successive acquired SAR data, the backscattered signals vary causing coherence degradation due to temporal decorrelations. This study estimated the coherence for all interferometric pairs to assess the temporal decorrelation effect and is expressed in Equation 4 (Ishitsuka *et al.*, 2012).

$$\gamma = \frac{|\sum_{n=1}^N P_1 P_2^* e^{i(\varphi_1 - \varphi_2)}|}{\sqrt{\sum_{n=1}^N |P_1|^2 \sum_{n=1}^N |P_2|^2}} \quad (4)$$

where N is the coherence window size. The similarity of pixels in a SAR product between master (pre-eruption image) and slave (post-eruption image) scenes is assessed using coherence. It ranges from zero (entirely dissimilar) to one (completely identical). When a natural hazard triggers a disaster, the paths of radar signals vary between two acquisition times over the same scatterer. Therefore, backscattered signals from vertically extending structures (e.g., buildings, houses, monuments, posts, etc.) and horizontally exposed linear systems (e.g., road networks) impaired after calamity results in coherence

degradation. Theoretically, the co-eruption event pair coherence (γ_{co}) would be lower than the pre-eruption event pair coherence (γ_{pre}). The difference (γ_{diff}) between the two coherence values is an asset to tracing affected regions due to the eruption on Taal Volcano island on January 12, 2020. The coherence difference was computed using Equation 5 (Ishitsuka *et al.*, 2012).

$$\gamma_{diff} = \gamma_{pre} - \gamma_{co} \quad (5)$$

All Sentinel-1 datasets before and after the eruptive activity acquired from both tracks were processed satisfying the presented equation above. Statistical manipulations to define a coherence difference threshold to trace modified surfaces due to the volcano eruption were applied to mitigate the background effects further (i.e., atmospheric effect and ordinal surface changes) (Ishitsuka *et al.*, 2012; Lu *et al.*, 2018). The details of interferometric pairs are summarized in Tables 2 and 3. In this study, the temporal and perpendicular baselines were controlled under 12 days and 150 m, respectively; thanks to the improved sampling frequency and orbital tube of the Sentinel-1 mission. The pre-eruption coherence difference data stack mean and standard deviation were exploited to achieve a coherence difference threshold for selecting pixels for creating DPM as defined in Equation 6.

$$\gamma_{diff}^{thre} < \gamma_{diff}^{mean} - \alpha \gamma_{diff}^{stddev} \text{ and } \gamma_{diff}^{thre} > \gamma_{diff}^{mean} + \alpha \gamma_{diff}^{stddev} \quad (6)$$

where γ_{diff}^{mean} and γ_{diff}^{stddev} are the pre-eruption coherence difference data stack mean and standard deviation. The coefficient α puts a weighting factor for standard deviation. This study adopted a threshold specifying $\alpha = 3$ (3-sigma), speculating a coherence difference normal distribution, which characterizes a remarkable surface change due to the eruption.

2.5 Ground Deformation Estimation using Differential InSAR (DInSAR)

InSAR analysis allows the estimation of ground deformations. This study used the co-eruption dataset from both tracks in this analysis from the phase difference information derived using two SAR images (i.e., one image before and after the eruption). First, coregistration of two SAR images was implemented after accurately updating the orbit data. Flat-earth and topographic phase errors were removed employing the POE data and Shuttle Radar Topography Mission (SRTM) DEM 1 arcsec data. Figure 3 displays the resulting differential interferograms for ascending and descending co-eruption interferometric pairs (see Table 1). The statistical-cost network-flow phase-

unwrapping algorithm (SNAPHU) program was used to unwrap the differential interferograms to retrieve the absolute interferometric phase values. The unwrapped interferograms were then converted to surface displacement measurements. A pixel with negligible surface displacement was selected as a stable reference area. This reference pixel has a coherence value close to 1.

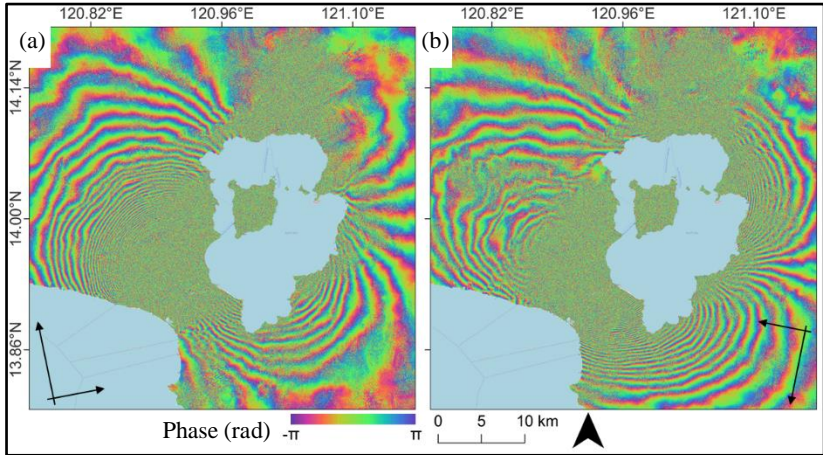


Figure 3. Co-ruption differential interferograms over Taal area were obtained from the ascending (a) and descending (b) interferometric pairs

It was noted that relative surface displacements were measured along the radar line-of-sight (LOS). Therefore, this study quantitatively decomposed the directional surface displacement involving the radar properties (look angle direction and incidence angle). East-west and vertical directional surface displacements decomposition were performed following the method of Fialko *et al.* (2001) as defined in Equations 7 and 8.

$$d_{LOS_A} = d_H \sin \theta_A + d_V \sin \theta_D \quad (7)$$

$$d_{LOS_D} = -d_H \sin \theta_D + d_V \sin \theta_A \quad (8)$$

where d_{LOS_A} and d_{LOS_D} are the LOS ascending and descending surface displacements, respectively. d_H and d_V provide the horizontal and vertical displacement components, respectively. θ_A and θ_D represent the incidence angles of the ascending and descending tracks, respectively. The resulting horizontal displacement component is comprised of two factors that are described in Equation 9.

$$d_H = d_{NS} \sin \delta - d_{EW} \sin \delta \quad (9)$$

where d_{NS} and d_{EW} are the N-S and E-W directional displacements, respectively and δ is the heading angle of both tracks. The heading angle of both tracks ranges from 0 to 180° concerning the vertical axis. Thus, the representation of the E-W component to horizontal displacement is more influential than that of the N-S component. In this study, it was assumed that the N-S component of the horizontal displacement was negligible since the heading angles of both tracks were less than 10°.

2.6 InSAR Results Validation and Assessment

On January 18, 2020, the PHIVOLCS Quick Response Team released a report presenting the documented fissures in different areas around Taal Volcano resulting from the recent eruption (PHIVOLCS, 2020). The report not only described the locations of the ground fissures but also detailed the vertical displacements. The geographical coordinates of the reported ground fissures were extracted from the report. Likewise, the research team conducted a field inspection on January 30, 2020 and documented other damages associated with the eruption besides ground fissures (i.e., cracks of buildings and houses). During the field inspection, vertical displacements were also measured using a tape measure (Figure 1e). The generated DPM and the estimated vertical displacements from InSAR were compared with documented damages and in-situ vertical measurements obtained from field inspection and PHIVOLCS reports. Cohen's kappa (k) statistic evaluated the validity of the DPM through interrater agreement using a confusion matrix. The minimum (MinDiff), maximum (MaxDiff) and mean (MeanDiff) of difference were all computed together with the root-mean-squared (RMS) and coefficient of determination (R^2) to check the authenticity of InSAR-derived ground deformations.

3. Results and Discussion

3.1 Spatial Distribution of Coherence Difference

Figures 4a to 4c display the pre-eruption coherence, co-eruption coherence and coherence difference maps produced after processing the interferometric pairs defined from the SAR images acquired by the ascending Sentinel-1 satellite. On the one hand, Figures 5a to 5c show the pre-eruption coherence, co-eruption coherence and coherence difference maps produced for the interferometric pairs derived after processing SAR images from the descending Sentinel-1 satellite.

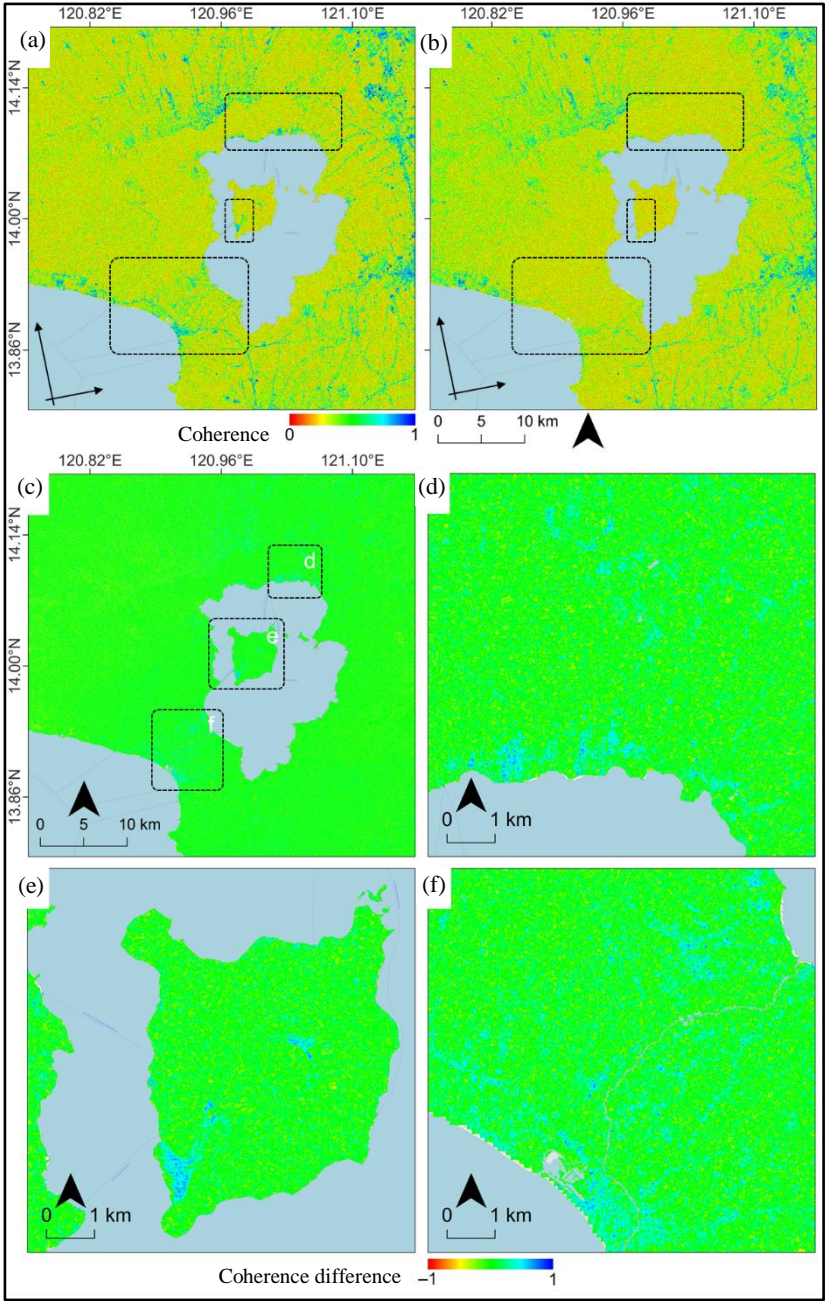


Figure 4. Pre-eruption coherence (a), co-eruption coherence (b) and coherence difference (c) maps for the ascending Sentinel-1 dataset. The enlarged portion of the regions (d-f) in (c).

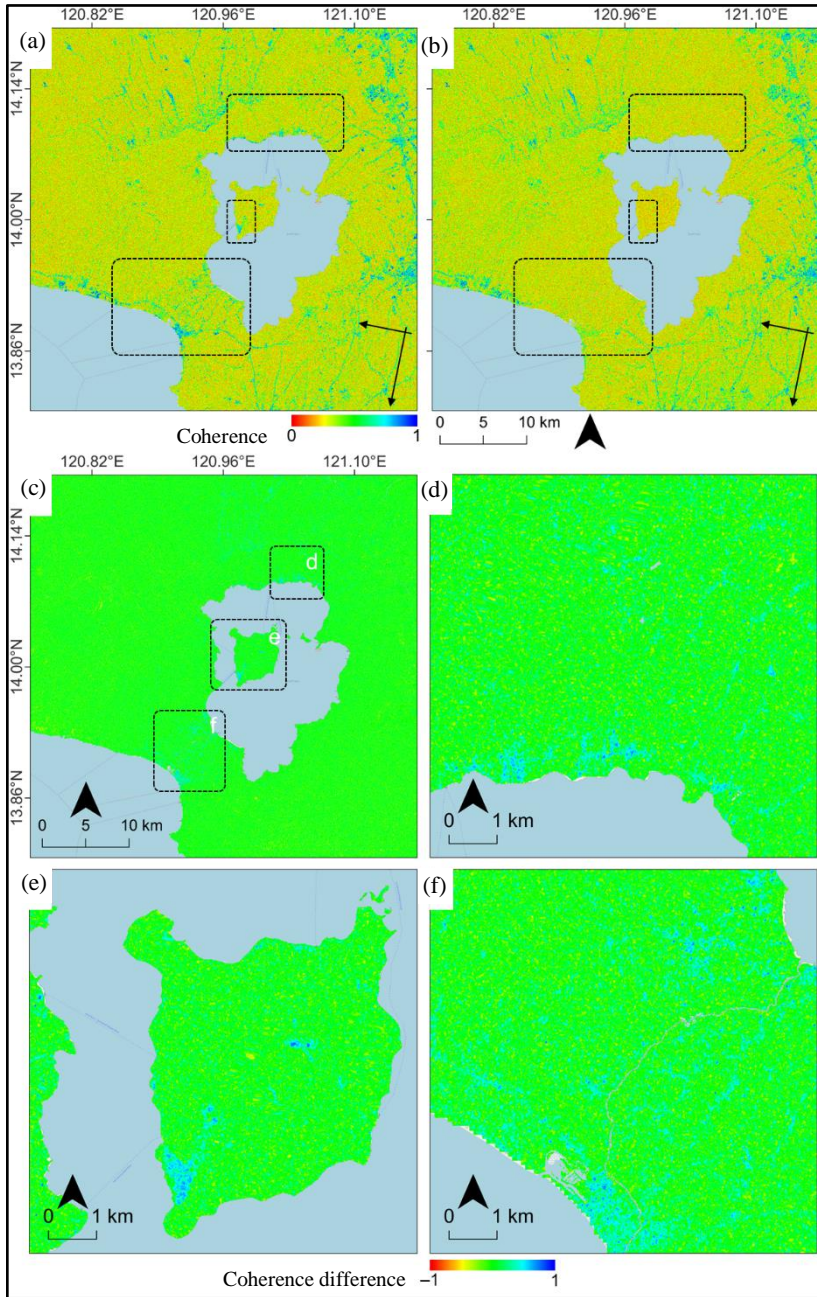


Figure 5. Pre-eruption coherence (a), co-eruption coherence (b) and coherence difference (c) maps for the descending Sentinel-1 dataset. The enlarged portion of the regions (d-f) in (c).

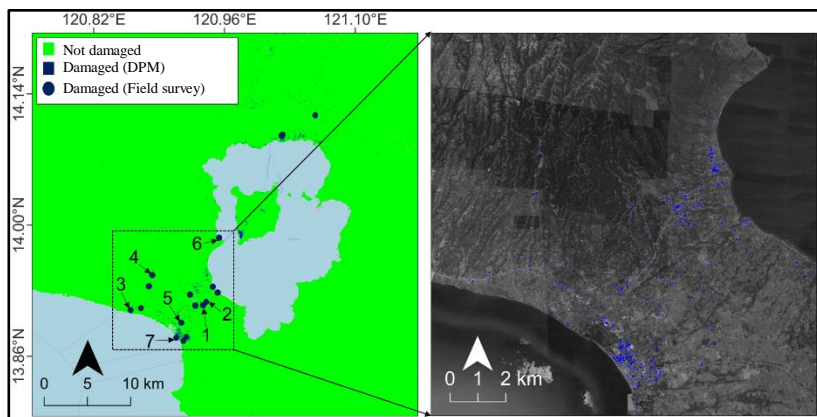
The blue and red variant tones represented regions with relatively high and low coherence, respectively. The co-eruption coherence of the regions emphasized by the hollow dashed black polygons from the ascending (Figure 4b) and descending (Figure 5b) tracks decreased appreciably relative to the pre-eruption coherence (Figures 4a and 5a) in most rural areas of Agoncillo, Lemery, San Nicolas, Taal and Talisay in Batangas. On one hand, the pre- and co-eruption coherence of interferometric pairs from the dataset acquired by the ascending and descending Sentinel-1 constellations for the other regions showed insignificant or no change. The coherence difference scale employing the concept in Equation 5 was between ± 1 . The coherence difference on the negative scale classified modified regions before the eruption but was unmodified during the eruption period. Likewise, the coherence difference on the positive scale classified modified regions during the eruption period but had marginal modifications before the eruption. The surface changes (i.e., damaged areas) in rural areas of the Batangas region emerged on the coherence difference maps from the two dataset sources were strongly positive (i.e., marked with hollow dashed black polygons in Figures 4c and 5c and the enlarged regions displayed in Figures 4d to 4f and Figures 5d to 5f) indicating the significant surface changes associated with the volcanic eruption. These surface changes were associated with large ground motions and volcanic ash deposits resulting in appreciable ground surface displacement and structural damage. Areas with the coherence difference near zero (i.e., green pixels) indicated regions with exact coherence across pre- and co-eruption interferometric pairs.

3.2 Validation of the Damage Proxy Map

In this study, the pre-eruption interferometric pair data stacks defined for the ascending and descending Sentinel-1 satellites were processed to mitigate the background effects. Coherence difference was calculated taking AP and DP (see Table 1) as reference pre-eruption interferometric pairs for the datasets acquired from the ascending and descending Sentinel-1 satellites, respectively. The mean and the standard deviation of the coherence difference of pre-eruption interferometric pairs stack were computed and exploited to achieve a coherence difference threshold according to Equation 6. The upper and lower bounds of the coherence difference threshold, calculated from the data stack of pre-eruption interferometric pairs from the two data sources, were identical. Note that the mean and standard deviation of pre-eruption coherence difference between the two data stacks were consistent. Pixels that satisfied the condition after applying the coherence difference threshold were

treated to have been significantly modified due to January 12, 2020, eruption on the Taal Volcano island.

Binary values (i.e., 0 and 1) were designated to each pixel over the study area after the thresholding. Green pixels had a value of 0 to represent areas that were not modified (or were removed after the thresholding) and blue pixels had a value of 1 to represent severely modified areas (or were selected after the thresholding). Figure 6 shows the DPM that integrated the two coherence difference maps from the two Sentinel-1 SAR data sources.



The blue area in the inset represents the integrated coherence difference maps from the two Sentinel-1 SAR data sources.

Figure 6. The damage proxy map (DPM) with the documented damaged areas from the PHIVOLCS report and the researchers' field survey

PHIVOLCS conducted field surveys to identify damaged areas in the 15-km danger zone after the eruption accompanied by volcanic earthquakes and released a report presenting the documented fissures and vertical displacement. The geographical coordinates of the documented damaged areas from the PHIVOLCS's report and the researchers' field survey, conducted on January 30, 2020, were collocated on Google Earth and overlaid with the produced DPM. The validity of the DPM was assessed using k . Table 4 lists the interrater (i.e., producer and user) reliability or interobserver agreement. Both observers rated four out of 18 surveyed sites as 'undetected' areas from the InSAR results. These four sites were in areas cloaked with trees; hence, they were masked using the coherence difference threshold (i.e., atmospheric and ordinal surface changes were believed to have affected these areas).

Table 4. Accuracy assessment using Cohen’s kappa statistics and confusion matrix

Class	Undetected areas	Detected areas	Sum	Producer’s accuracy
Undetected areas	4	2	6	0.67
Detected areas	0	12	12	1.00
Sum	4	14	Overall accuracy is 89%	
User’s accuracy	1.00	0.86	Cohen’s kappa k is 0.73	

Moreover, both observers rated 12 out of 18 surveyed as ‘detected’ areas from the InSAR results. These 12 sites were found to be houses and roads that were damaged due to the eruption. The calculated k value was 0.73 indicating a robust interrater agreement. The accuracy was 89% after comparing the DPM with the documented ground fissures using the confusion matrix (see Table 4). This accuracy suggested that the created DPM traced the documented fissures reported by the group and PHIVOLCS, especially in rural areas near the Pansipit River.

Besides the recent Taal Volcano eruption, the Philippines also experienced earthquakes of varying magnitudes in the last decade damaging buildings, houses and roads and leading to the loss of human lives. In these past events, InSAR was not commonly utilized to investigate the resulting ground motions and their associated damages to assets. The only earthquake-related InSAR applications were found for the 2019 Mindanao earthquake sequence (Li *et al.*, 2020), the 2019 Zambales earthquake (Abcede *et al.*, 2022) and the 2020 Masbate earthquake (Tiongson and Ramirez, 2022). Of these three previous studies, Tiongson and Ramirez (2022) and Abcede *et al.* (2022) employed the coherence difference analysis to map damaged structural and non-structural assets incurred after the earthquake events aside from quantifying the ground surface displacements. These two previous studies adapted the two-step coherence threshold workflow by Lu *et al.* (2018) to refine the coherence difference by utilizing a stack of coherence data from pre-event images. The coherence difference from these studies was calculated similarly by subtracting the co-event coherence from the pre-event coherence. This study only adapted the single-step coherence thresholding by Ishitsuka *et al.* (2012). It is worth noting that Ishitsuka *et al.* (2012) and Lu *et al.* (2018) shared the exact utilization of the mean and standard deviation of coherence data from the pre-event image stack. However, Lu *et al.* (2018) integrated the use of temporal or natural coherence decay to refine further the mitigation of background noise and ordinal surface changes. Ishitsuka *et al.* (2012) obtained

85 and 61% detection accuracy in areas affected by liquefaction in Tokyo Bay and Tone River in Japan, respectively. Tiongson and Ramirez (2022) and Abcede *et al.* (2022) showed promising results despite some documented asset damages not successfully mapped by the final coherence difference map. This mismatch might be attributed to the inability of the analysis method to identify small damaged assets relative to the spatial resolution of the processed Sentinel-1 SAR images.

3.3 Spatial Distribution of Ground Surface Displacement

Figure 3 displays the two co-eruption differential interferograms generated for the processed SAR images acquired by the ascending and descending Sentinel-1 satellites (see Table 1). Interferometric fringes reflected the ground surface displacements in the satellite radar LOS. One interferometric fringe cycle in the case of Sentinel-1 was equal to 2.8 cm. The interferograms revealed noticeable co-eruption surface displacement along the satellite LOS. Tight interferometric fringes over the Batangas region corresponded to strong ground motion associated with the volcanic eruption. Different ground motion patterns (i.e., fringes) were notable from the two differential interferograms in ascending and descending modes. These different fringe patterns meant that an appreciable horizontal motion component (i.e., in the east-west direction) was contained in the LOS displacement field. In the case of pure vertical ground surface displacement (i.e., up-down movement), the differential interferograms generated for the two data sources would show similar interferometric fringes. The LOS displacement field map presented in Figure 7 supports this observation. Note that positive displacement (cold color) indicated movement towards the sensor, while negative displacement (warm color) represented a movement away from the sensor. The southwest portion of the examined area moved closer to the ascending sensor and away from the descending sensor. Moreover, the southeast region of Taal moved away from the ascending radar and closer to the descending radar.

The horizontal (east-west) and vertical (up-down) motions were quantified around the active volcano after employing Equations 7 and 8. The distributions of east-west and vertical surface displacements are presented in Figure 8. The color scale bar for the east-west directional component was -1 m to 1 m, whereas, for the vertical component, the color scale bar was from -0.6 m to 0.6 m. The directional components of the displacement revealed that the horizontal motion was more significant than the vertical motion. The east-west component showed that the southwest portion of Taal moved away from

the eastern side indicating land extension. This event could explain the appearance of fissures or cracks in the proximity of the Pansipit River, which serves as a drainage outlet of Taal lake, causing damage to buildings and road pavements. This extension was accompanied by vertical displacement (uplift) due to the upward movement of the magma towards the main crater. It is unclear, however, for the authors if volcanic earthquakes are the main actors for fissures or surface crack formations, although they may very well be in some instances. The ground deformation patterns during volcanic unrest and the accompanying earthquakes certainly played a role in generating surface cracks.

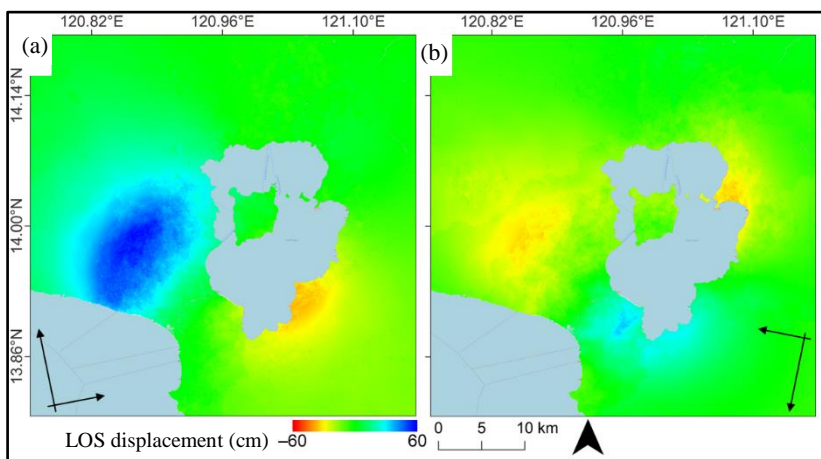


Figure 7. The LOS displacement map in the Taal area: results of (a) ascending image and (b) descending image pairs

As mentioned previously, Morales Rivera *et al.* (2015) processed nearly 20 ALOS-1 SAR images acquired during 2007-2011 to monitor four active volcanoes in the Philippines, including the Taal Volcano, and model their deformation characteristics related to changes in pressurization of the system. Morales Rivera *et al.* (2015) found that the LOS velocity increased positively (i.e., uplift and westing) between February 2010 and January 2011 at a maximum displacement rate of 14.1 cm/yr. This increase extended to the western shore of Taal Lake and was consistent with the movements observed in this study after processing SAR images acquired by the ascending and descending Sentinel-1 satellites. Likewise, almost the same deformation patterns (i.e., horizontal east-west and vertical up-down movements) were reported by Bato *et al.* (2021), except in a few areas in the immediate adjoining west region of the Pansipit River Valley after processing Sentinel-1 SAR

images. It is worth noting that Bato *et al.* (2021) also employed a pixel offset (PO) analysis besides InSAR to detect the large deformation within the Taal Volcano and the Pansipit River Valley associated with the recent volcano eruption. The large deformations in these areas resulted in significant coherence loss; thus, non-inclusion of incoherent pixels for ground surface deformation estimation. However, displacement estimates from PO analysis have lower accuracy than InSAR measurements.

Nevertheless, the observed positive increase in the displacement rate on the southwest region of Taal Volcano island is likely attributed to the inflation caused by the pressurization of the volcanic system (Morales Rivera *et al.*, 2015). On the other hand, deflation was observed in the northeast region of Taal Volcano island, which is consistent with previous studies. Moreover, Mabaquiao (2021) processed two Sentinel-1 SAR images and reported ground surface deformation in Metro Manila between -4.7 cm (i.e., subsidence) and +9.6 cm (i.e., uplift) after the 2020 Taal Volcano eruption.

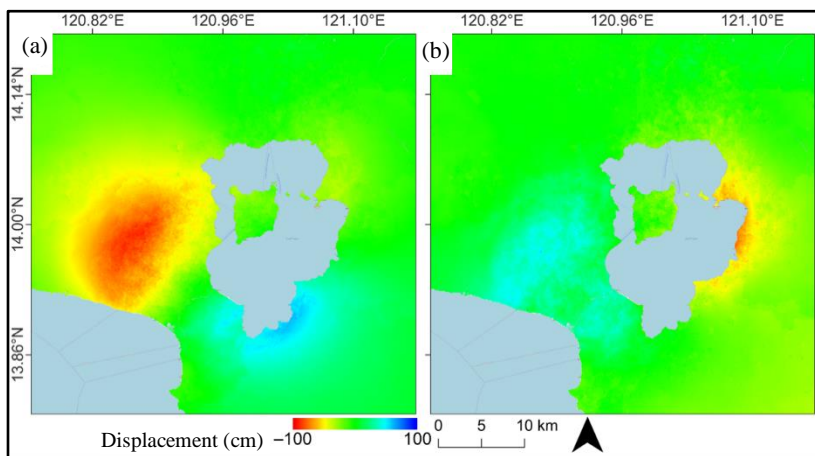


Figure 8. Decomposed LOS surface displacements; the spatial distribution of horizontal (i.e., east-west) (a) and vertical (i.e., up-down) directional (b) surface displacements

3.4 Comparison with Field Survey Reports

The research group and PHIVOLCS independently measured and recorded the vertical displacement of surveyed sites after the January 12, 2020 eruption. The vertical displacements were measured between January 18, 2020 and January 30, 2020. Seven out of 18 surveyed sites showed minimum and maximum vertical displacements of 5 and 60 cm, respectively. Measurement

points used for comparison were marked with numbers 1 through 7 in Figure 6. The comparison of vertical displacements derived from the field and DInSAR data, as shown in Table 5, revealed that the absolute error or difference was less than 2 cm. The 2-cm discrepancy can be attributed to the phase errors (i.e., atmospheric and DEM errors) that were not totally mitigated from the InSAR products as the current processing tool does not incorporate atmospheric phase screen (APS) estimation and removal. Moreover, the results showed that the RMS and R^2 were 1.65 cm and 0.99, respectively, confirming the DInSAR-derived vertical displacement results (Figure 9).

Table 5. Comparison of vertical displacement from in-situ and DInSAR data

Site no.	DInSAR measured (cm)	In-situ measured (cm)	Difference (cm)	MinDiff (cm)	MaxDiff (cm)	MeanDiff (cm)	RMS (cm)	R^2
1	36.24	35	1.24					
2	25.86	24	1.86					
3	38.20	40	-1.80					
4	30.45	29	1.45	-1.80	1.84	1.64	1.65	0.99
5	9.35	7.5	1.85					
6	33.40	35	-1.60					
7	48.35	50	-1.65					

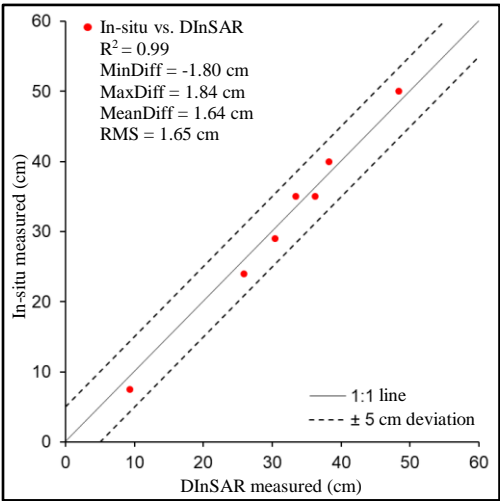


Figure 9. Comparison of vertical displacement from in-situ and DInSAR data

4. Conclusion and Recommendation

In this study, the applied InSAR technique delineated the changes in the surfaces of ground targets due to the Taal Volcano eruption in the Philippines on January 12, 2020 using the coherence difference analysis between pre-eruption and co-eruption interferometric pairs of SAR images acquired by the ascending and descending Sentinel-1 mission. The InSAR results presented the successful utilization of the pre-eruption coherence difference data stack mean and the standard deviation in defining a coherence difference threshold to arrest the strong temporally decorrelated radar signal related to the phreatomagmatic eruption and volcanic earthquakes. The applied technique also decomposed horizontal (i.e., east-west) and vertical (i.e., up-down) directional components of ground surface displacements using InSAR analysis by unwrapping the co-eruption differential interferograms. The InSAR-derived vertical displacements associated with the 2020 Taal Volcano eruption were between 9 to 50 cm. The InSAR-based outcomes were consistent with in-situ surveys and displacement measurements with an overall accuracy of 89% for damaged area mapping using DPM and $RMS < 2$ cm and R^2 of 0.99 for the ground displacement estimation. Therefore, these surface changes traced through the InSAR phase and coherence change detection methods were linked to Taal volcano's recent phreatomagmatic eruption accompanied by volcanic earthquakes. This study presented that Sentinel-1 SAR data with medium spatial resolution acquired with a shorter revisit period over the same region was efficient for mapping damaged areas and estimating ground surface displacements.

This study presented the usefulness of using medium-resolution C-band Sentinel-1 SAR images for mapping damaged areas and estimating ground surface deformations due to the 2020 Taal Volcano phreatomagmatic eruption accompanied by volcanic earthquakes. The InSAR change detection methods adequately produced reasonable DPM and ground surface displacement estimates compared with ground truth acquired from field surveys and PHIVOLCS reports but still face some limitations. The number of Sentinel-1 SAR images acquired before the volcano eruption, covering approximately six months, may not be sufficient to define the optimal coherence difference threshold calculated using the mean and standard deviation of pre-eruption coherence data. Note that for each Sentinel-1 orbit, only 16 SAR images were collected for this study and each image acquisition was 12-days apart. However, as Sentinel-1 provides images acquired every six days in other regions and recently in the Philippines, the increased archived database can

provide better pre-event natural coherence variability, specifically in densely vegetated and rural areas. In addition, Sentinel-1 provides medium-resolution SAR images, specifically with a nominal spatial resolution of 5 x 20 m (range x azimuth). This spatial resolution limits the capability of the coherence difference analysis method to identify small damaged structural and non-structural assets assuming that the asset only belongs to one pixel. It is worth noting that in exchange for better coherence and reduced speckle noise, multilooking was performed, which degraded the original spatial resolution of the Sentinel-1 SAR datasets. Using higher resolutions SAR images acquired by TerraSAR-X (i.e., 2 x 3.3 m, range x azimuth) and COSMO-SkyMed (i.e., 2.21 x 1.63 m, range x azimuth) can improve the detection of small damaged assets; however, there is a cost associated.

Moreover, the ineffective removal of other phase components, specifically the atmospheric phase contribution, introduces significant errors when using conventional InSAR methods, which are in the order of a centimeter. In this case, advanced InSAR time series techniques can be employed such as the Persistent Scatterer InSAR (PS-InSAR) and the Small Baseline Subset (SBAS). These advanced InSAR time series techniques can mitigate the shortcomings of the conventional InSAR.

5. Acknowledgement

The authors would like to thank to the European Space Agency (ESA) and European Commission (EC) for freely distributing Sentinel-1 SAR images under the Copernicus Programme. The authors also thank the United States Geological Survey (USGS) in cooperation with the National Aeronautics and Space Administration (NASA) for providing the SRTM DEM 1 arcsec data.

6. References

Abcede, E.L., Ajesta, A., Alfonso, J.D., Nucup, R.J., Peralta, M., & Ramirez, R. (2022). InSAR-based detection and mapping of seismically induced ground surface displacement and damage in Pampanga, Philippines. *ASEAN Engineering Journal*, 12(2), 1-10. <https://doi.org/10.11113/aej.v12.16496>

Baker, S., & Amelung, F. (2012). Top-down inflation and deflation at the summit of Kilauea Volcano, Hawai'i observed with InSAR. *Journal of Geophysical Research: Solid Earth*, 117(B12), 1-14. <https://doi.org/10.1029/2011JB009123>

Bato, M.G., Lundgren, P., Pinel, V., Solidum, R., Jr., Daag, A., & Cahulogan, M. (2021). The 2020 eruption and large lateral dike emplacement at Taal Volcano, Philippines: Insights from satellite radar data. *Geophysical Research Letters*, 48(7), e2021GL092803. <https://doi.org/10.1029/2021GL092803>

Bartel, B.A., Hamburger, M.W., Meertens, C.M., Lowry, A.R., & Corpuz, E. (2003). Dynamics of active magmatic and hydrothermal systems at Taal Volcano, Philippines, from continuous GPS measurements. *Journal of Geophysical Research: Solid Earth*, 108(B10), 1-15. <https://doi.org/10.1029/2002JB002194>

Bürgmann, R., Rosen, P.A., & Fielding, E.J. (2000). Synthetic aperture radar interferometry to measure earth's surface topography and its deformation. *Annual Review of Earth and Planetary Science*, 28, 169-209. <https://doi.org/10.1146/annurev.earth.28.1.169>

Chen, Q., Liu, X., Zhang, Y., Zhao, J., Xu, Q., Yang, Y., & Liu, G. (2019). A nonlinear inversion of InSAR-observed coseismic surface deformation for estimating variable fault dips in the 2008 Wenchuan earthquake. *International Journal of Applied Earth Observation and Geoinformation*, 76, 179-192. <https://doi.org/10.1016/j.jag.2018.10.022>

Delos Reyes, P.J., Bornas, M.A.V., Dominey-Howes, D., Pidlaon, A.C., Magill, C.R., & Solidum, R.U. (2018). A synthesis and review of historical eruptions at Taal Volcano, Southern Luzon, Philippines. *Earth-Science Reviews*, 177, 565-588. <https://doi.org/10.1016/j.earscirev.2017.11.014>

Di Traglia, F., De Luca, C., Manzo, M., Nolesini, T., Casagli, N., Lanari, R., & Casu, F. (2021). Joint exploitation of space-borne and ground-based multitemporal InSAR measurements for volcano monitoring: The Stromboli volcano case study. *Remote Sensing of Environment*, 260, 112441. <https://doi.org/10.1016/j.rse.2021.112441>

Doke, R., Harada, M., Mannen, K., Itadera, K., & Takenaka, J. (2018). InSAR analysis for detecting the route of hydrothermal fluid to the surface during the 2015 phreatic eruption of Hakone Volcano, Japan. *Earth, Planets and Space*, 70, 63. <https://doi.org/10.1186/s40623-018-0834-4>

Ebmeier, S.K., Andrews, B.J., Araya, M.C., Arnold, D.W.D., Biggs, J., Cooper, C., Cottrell, E., Furtney, M., Hickey, J., Jay, J., Lloyd, R., Parker, A.L., Pritchard, M.E., Robertson, E., Venzke, E., & Williamson, J.L. (2018). Synthesis of global satellite observations of magmatic and volcanic deformation: Implications for volcano monitoring and the lateral extent of magnetic domains. *Journal of Applied Volcanology*, 7, 2. <https://doi.org/10.1186/s13617-018-0071-3>

Fernández, J., Romero, R., Carrasco, D., Luzón, F., & Araña, V. (2002). InSAR volcano and seismic monitoring in Spain. Results for the period 1992-2000 and possible interpretations. *Optics and Lasers in Engineering*, 37(2-3), 285-297. [https://doi.org/10.1016/S0143-8166\(01\)00085-9](https://doi.org/10.1016/S0143-8166(01)00085-9)

Fialko, Y., Simons, M., & Agnew, D. (2001). The complete (3-D) surface displacement field in the epicentral area of the 1999 Mw 7.1 Hector Mine earthquake, California, from space geodetic observations. *Geophysical Research Letters*, 28(16), 3063-3066. <https://doi.org/10.1029/2001GL013174>

Fikos, I., Vargemezis, G., Zlotnicki, J., Puertollano, J.R., Alanis, P.B., Pigtain, R.C., Villacorte, E.U., Malipot, G.A., & Sasai, Y. (2012). Electrical resistivity tomography study of Taal volcano hydrothermal system, Philippines. *Bulletin of Volcanology*, 74, 1821-1831. <https://doi.org/10.1007/s00445-012-0638-5>

Galgana, G.A., Newman, A.V., Hamburger, M.W., & Solidum, R.U. (2014). Geodetic observations and modeling of time-varying deformation at Taal Volcano, Philippines. *Journal of Volcanology and Geothermal Research*, 271, 11-23. <https://doi.org/10.1016/j.jvolgeores.2013.11.005>

Garthwaite, M.N., Miller, V.L., Saunders, S., Parks, M.M., Hu, G., & Parker, A.L. (2019). A simplified approach to operational InSAR monitoring of volcano deformation in low- and middle-income countries: Case study of Rabaul Caldera, Papua New Guinea. *Frontiers in Earth Science*, 6, 240. <https://doi.org/10.3389/feart.2018.00240>

Google. (n.d.). Taal Volcano Island Google Earth satellite image. Retrieved from <https://www.google.com/maps/@14.0165399,121.0118383,27411m/data=!3m1!1e3>

Hamling, I.J. (2021). InSAR observations over the Taupō Volcanic Zone's cone volcanoes: Insights and challenges from the New Zealand volcano supersite. *New Zealand Journal of Geology and Geophysics*, 64(2-3), 347-357. <https://doi.org/10.1080/00288306.2020.1721545>

Ishitsuka, K., Tsuji, T., & Matsuoka, T. (2012). Detection and mapping of soil liquefaction in the 2011 Tohoku earthquake using SAR interferometry. *Earth, Planets and Space*, 64, 1267-1276. <https://doi.org/10.5047/eps.2012.11.002>

Jung, J., Kim, D.J., Lavallo, M., & Yun, S.H. (2016). Coherent change detection using InSAR temporal decorrelation model: A case study for the volcanic ash detection. *IEEE Transactions on Geoscience and Remote Sensing*, 54(10), 5765-5775. <https://doi.org/10.1109/TGRS.2016.2572166>

Kubaneck, J., Richardson, J.A., Charbonnier, S.J., & Connor, L.J. (2015). Lava flow mapping and volume calculations for the 2012-2013 Tolbachik, Kamchatka, fissure eruption using bistatic TanDEM-X InSAR. *Bulletin of Volcanology*, 77, 106. <https://doi.org/10.1007/s00445-015-0989-9>

Kumagai, H., Lacson R., Jr., Maeda, Y., Figueroa, M.S., II, & Yamashina, T. (2014). Shallow S wave attenuation and actively degassing magma beneath Taal Volcano, Philippines. *Geophysical Research Letters*, 41(19), 6681-6688. <https://doi.org/10.1002/2014GL061193>

Li, B., Li, Y., Jiang, W., Su., Z., & Shen, W. (2020). Conjugate ruptures and seismotectonic implications of the 2019 Mindanao earthquake sequence inferred from Sentinel-1 InSAR data. *International Journal of Applied Earth Observation and Geoinformation*, 90, 102127. <https://doi.org/10.1016/j.jag.2020.102127>

Liu, F., Elliot, J.R., Craig, T.J., Hooper, A., & Wright, T.J. (2021). Improving the resolving power of InSAR for earthquakes using time series: A case study in Iran. *Geophysical Research Letters*, 48(14), e2021GL093043. <https://doi.org/10.1029/2021GL093043>

Lowry, A.R., Hamburger, M.W., Meertens, C.M., & Ramos, E.G. (2001). GPS monitoring of crustal deformation at Taal Volcano, Philippines. *Journal of Volcanology and Geothermal Research*, 105(1-2), 35-47. [https://doi.org/10.1016/S0377-0273\(00\)00238-9](https://doi.org/10.1016/S0377-0273(00)00238-9)

Lu, C.H., Ni, C.F., Chang, C.P., Yen, J.Y., & Chuang, R.Y. (2018). Coherence difference analysis of Sentinel-1 SAR interferograms to identify earthquake-induced disasters in urban areas. *Remote Sensing*, 10(8), 1318. <https://doi.org/10.3390/rs10081318>

Mabaquiao, L.C. (2021). InSAR-based LOS surface deformation comparison of Metro Manila before and after the January 2020 Taal Volcano eruption. *Proceedings of the International Archives of the Photogrammetry, Remote Sensing and Spatial Information Sciences, Virtual Meeting*, 201-206.

Massonnet, D., & Sigmundsson, F. (2000). Remote sensing of volcano deformation by radar interferometry from various satellites. *Remote Sensing of Active Volcanism*, 116, 207-221. <https://doi.org/10.1029/GM116p0207>

Morales Rivera, A.M., Amelung, F., & Eco, R. (2015). Volcano deformation and modeling on active volcanoes in the Philippines from ALOS InSAR time series. *Proceedings of FRINGE'15: Advances in the Science and Applications of SAR Interferometry and Sentinel-1 InSAR Workshop*, Frascati, Italy, 1-6.

Moro, M., Saroli, M., Stramondo, S., Bignami, C., Albano, M., Falcucci, E., Gori, S., Doglioni, C., Polcari, M., Tallini, M., Macerola, L., Novali, F., Costantini, M., Malvarosa, F., & Wegmüller, U. (2017). New insights into earthquakes precursors from InSAR. *Scientific Reports*, 7, 12035. <https://doi.org/10.1038/s41598-017-12058-3>

Nobile, A., Acocella, V., Ruch, J., Aoki, Y., Borgstrom, S., Siniscalchi, V., & Geshi, N. (2017). Steady subsidence of a repeatedly erupting caldera through InSAR observations: Aso, Japan. *Bulletin of Volcanology*, 79, 32. <https://doi.org/10.1007/s00445-017-1112-1>

Philippine Institute of Volcanology and Seismology (PHIVOLCS). (2019). Taal Volcano Bulletin 28 March 2019 9:15 am. Retrieved from <https://www.phivolcs.dost.gov.ph/index.php/taal-volcano-bulletin-menu/8117-taal-volcano-bulletin-28-march-2019-9-15-am-2>

Philippine Institute of Volcanology and Seismology (PHIVOLCS). (2020). General location of fissures related to the January 2020 Taal Volcano eruptive activity. Retrieved from <https://www.phivolcs.dost.gov.ph/index.php/news/9662-general-location-of-fissures-related-to-the-january-2020-taal-volcano-eruptive-activity>

Prasetyo, Y.T., Kurata, Y.B., Acosta, A.R., Aben, A.P.F.B., Persada, S.F., Nadlifatin, R., & Redi, A.A.N.P. (2021). Factors affecting response actions of the 2020 Taal Volcano eruption among Filipinos in Luzon, Philippines: A structural equation

modeling approach. *International Journal of Disaster Risk Reduction*, 63, 102454. <https://doi.org/10.1016/j.ijdr.2021.102454>

Ramirez, R. (2021). The application of interferometric synthetic aperture radar (InSAR) on damaged area mapping: The case of the 2020 Taal Volcano eruption. *Proceedings of the 2021 IEEE International Geoscience and Remote Sensing Symposium (IGARSS)*, Brussels, Belgium, 5342-5345.

Strozzi, Y., Luckman, A., Murray, T., Wegmüller, U., & Werner, C.L. (2002). Glacier motion estimation using SAR offset-tracking procedures. *IEEE Transactions on Geoscience and Remote Sensing*, 40(11), 2384-2391. <https://doi.org/10.1109/TGRS.2002.805079>

Tiongson, S.F., & Ramirez, R. (2022). Mapping of ground surface deformations and its associated damage using SAR interferometry: A case study of the 2020 Masbate earthquake. *E3S Web of Conferences*, 347, 03014. <https://doi.org/10.1051/e3sconf/202234703014>

Wang, T., DeGrandpre, K., Lu, Z., & Freymueller, J.T. (2018). Complex surface deformation of Akutan Volcano, Alaska revealed from InSAR time series. *International Journal of Applied Earth Observation and Geoinformation*, 64, 171-180. <https://doi.org/10.1016/j.jag.2017.09.001>

Wauthier, C., Cayol, W., Kervyn, F., & d'Oreye, N. (2009). The January 2002 eruption of Nyiragongo Volcano (DRC) captured by InSAR. *Proceedings of the IEEE International Geoscience and Remote Sensing Symposium (IGARSS)*, Cape Town, South Africa, 416-419.

Zebker, H.A., Amelung, F., & Jónsson, S. (2000). Remote sensing of volcano surface and internal processes using radar interferometry. *Remote Sensing of Active Volcanism*, 116, 179-205. <https://doi.org/10.1029/GM116p0179>

Zlotnicki, J., Vargemezis, G., Johnston, M.J.S., Sasai, Y., Reniva, P., & Alanis, P. (2017). Very-low-frequency resistivity, self-potential and ground temperature surveys on Taal Volcano (Philippines): Implications for future activity. *Journal of Volcanology and Geothermal Research*, 340, 180-197. <https://doi.org/10.1016/j.jvolgeores.2017.04.020>